Promotion and suppression of single-molecule conductance by quantum interference in macrocyclic circuits

Hongliang Chen[1,2,6,7], Songjun Hou[3,7], Qingqing Wu[3], Feng Jiang[4], Ping Zhou[4], Long Zhang[2], Yang Jiao[2], Bo Song[2], Qing-Hui Guo[1,2,6], Xiao-Yang Chen[2], Wenjing Hong[4,*], Colin J. Lambert[3,*], and J. Fraser Stoddart[1,2,5,6,8,*]

[1]Department of Chemistry, Northwestern University, 2145 Sheridan Road, Evanston, IL 60208, USA

[2]Stoddart Institute of Molecular Science, Department of Chemistry, Zhejiang University, Hangzhou 310021, China

[3]Department of Physics, Lancaster University, Lancaster LA1 4YB, UK

[4]State Key Laboratory of Physical Chemistry of Solid Surfaces, iChEM, College of Chemistry and Chemical Engineering, Xiamen University, Xiamen 361005, China

[5]School of Chemistry, University of New South Wales, Sydney, NSW 2052, Australia

[6]ZJU-Hangzhou Global Scientific and Technological Innovation Center, Hangzhou 311215, China

[7]These authors contributed equally: H. Chen, S. Hou.

[8]Lead Contact

*Correspondence: whong@xmu.edu.cn (W.H.); c.lambert@lancaster.ac.uk (C.J.L); stoddart@northwestern.edu (J.F.S.)

SUMMARY

Single-molecule electronics is a sub-field of nanoelectronics, in which the individual devices are formed from single molecules placed between source and drain electrodes. During the past few years, both theory and experiment have demonstrated that that the flow of electricity through such devices is controlled by quantum interference (QI) between electrons passing from the source to the drain, but their future development is currently hampered by the difficulties in controlling such interference effects. Herein, we demonstrate a modular design of single-molecule circuits, which enable the construction of basic electronic components — namely, conductors or insulators — based on one tetracationic cyclophane platform. We demonstrate that the electron transport in cyclophane circuits is mediated by QI between channels formed from two lowest unoccupied molecular orbitals (LUMOs), while their highest occupied molecular orbitals (HOMOs) play no significant role. We further reveal that energy differences between these two LUMO channels induce constructive interference, leading to high conductance. By contrast, the phase differences between these LUMO channels result in destructive interference and a suppression in the overall conductance.

KEYWORDS

Cyclophanes; intramolecular circuits; LUMO-dominated transport; molecular electronics; quantum interference; single-supermolecule electronics; STM–BJs

INTRODUCTION

A cornerstone of the molecular electronics[1-3] is the use of one single-molecule platform to construct[4-8] different electronic components. A common strategy is to manipulate the quantum interference[9-11] (QI) which takes place between molecular orbitals whose energies are close to the electrode Fermi energy, E_F. It is, however, challenging to align[12-16] the energies of these frontier orbitals relative to the E_F. The conductance of a ring-shaped mesoscopic structure can be

manipulated[17,18] through QI between the de Broglie waves of electrons traversing the two branches of the loop structure — i.e., conductance is enhanced by constructive quantum interference (CQI) and suppressed when destructive quantum interference (DQI) occurs. The concept of using CQI and DQI to control the flow of electricity through single molecules was proposed theoretically[19-23] since 1988 and demonstrated experimentally[14,24,25] in 2011. The QI control strategy also applies[26-28] to large macrocyclic junctions, where the parallel transport paths have lengths much greater than the de Broglie wavelength of the tunneling electrons. In 2012, experimental evidence[15] was presented for a proposed superposition law[29] for these macrocyclic junctions, which predicts (**equation 1**) CQI for a cyclophane with two parallel electron transport channels, compared with its single-channel counterpart, i.e., one half of the cyclophane. However, as demonstrated below, DQI between two channels[30,31], may result in significant modifications to this superposition law.

Herein, we describe the synthesis of a series of very weakly coupled two-channel cyclophanes to overcome this barrier. We demonstrate that both CQI and DQI can be achieved by manipulating the interplay between these two channels. In order to facilitate this tuning, electron withdrawing units have been included in the design of our molecules, leading to LUMO-dominated transport and the switching between CQI and DQI by simple manipulation (**Figure 1A**) of the LUMO on one of the two conducting channels. From a fundamental point of view, this investigation will also reveal that conductance ratios can be far higher or far lower than the value of 4 predicted by the single-molecule superposition law.[29]

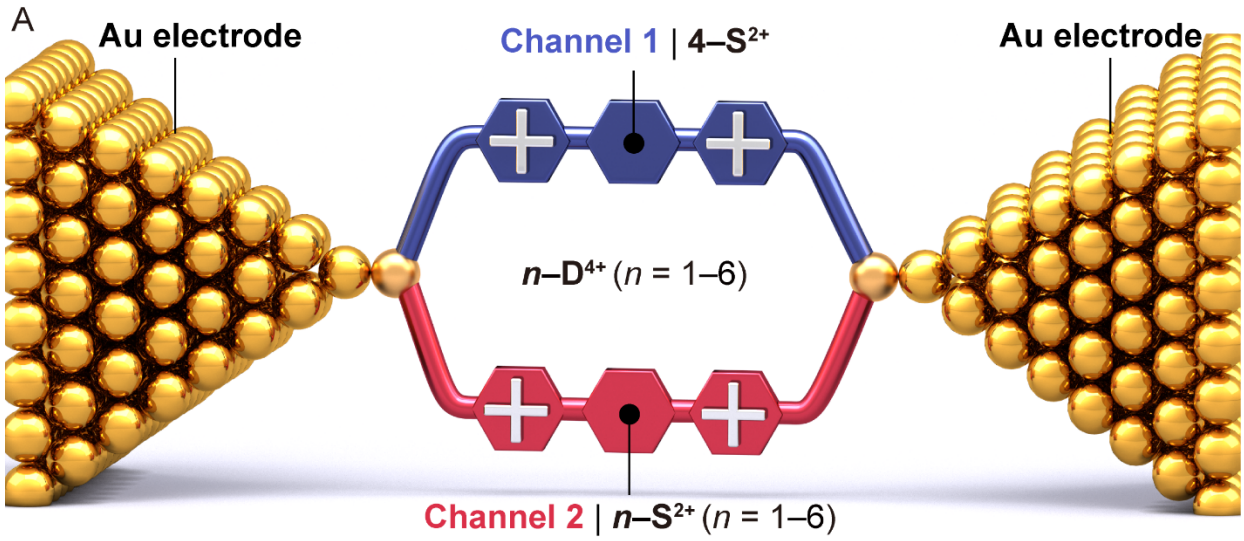
A
Au electrode
Channel 1 | 4–S2+
Au electrode
n–D4+ (n = 1–6)
Channel 2 | n–S2+ (n = 1–6)

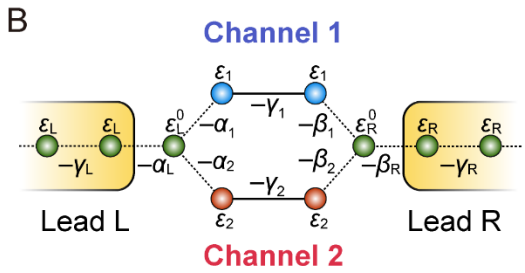
B
Channel 1
Lead L
Lead R
Channel 2

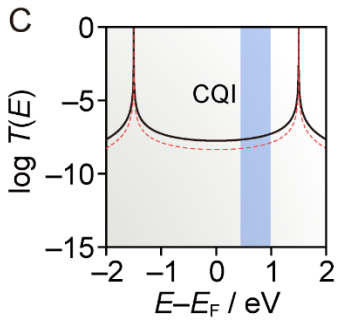
C
CQI
log T(E)
E–EF / eV

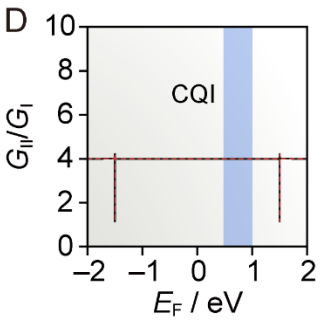
D
CQI
GII/GI
EF / eV

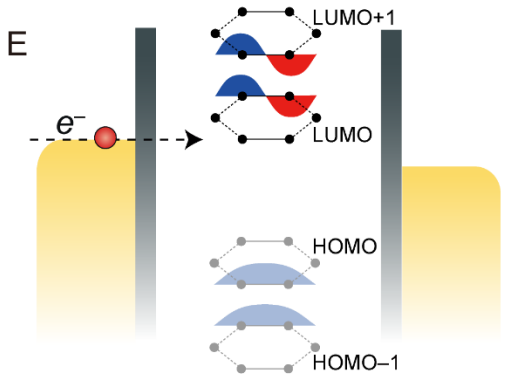
E
e–
LUMO+1
LUMO
HOMO
HOMO–1

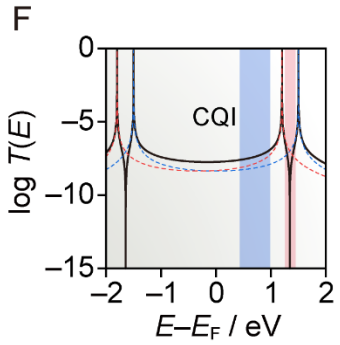
F
CQI
log T(E)
E–EF / eV

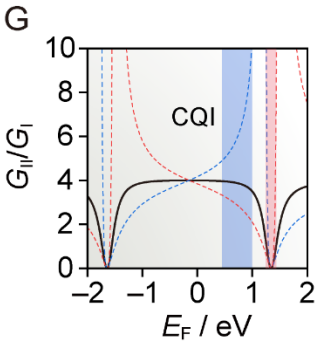
G
CQI
GII/GI
EF / eV

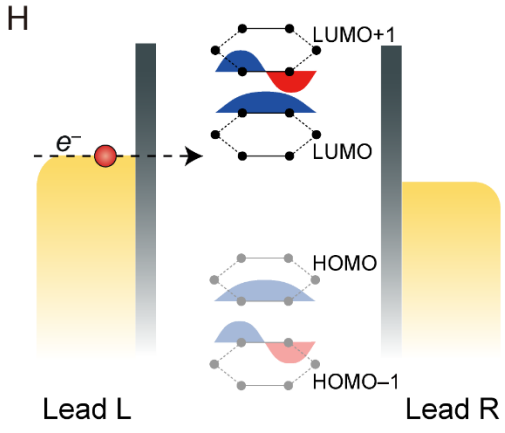
H
e–
LUMO+1
LUMO
HOMO
HOMO–1
Lead L
Lead R

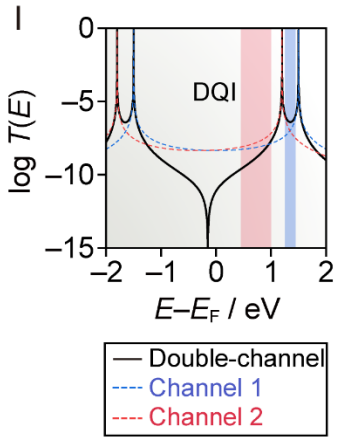
I
DQI
log T(E)
E–EF / eV
Double-channel
Channel 1
Channel 2

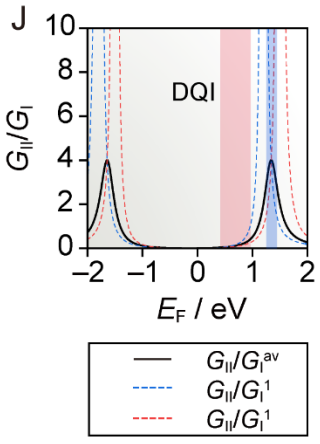
J
DQI
GII/GI
EF / eV
GII/GIav
GII/GI1
GII/GI1

Figure 1 | LUMO-Mediated CQI and DQI in Single-Molecule Macrocyclic Circuits

(A) Schematic illustration showing an asymmetric cyclophane circuit, ***n*–D^{4+}** (n = 1−6). The counterions are omitted for the sake of clarity.

(B) A two-channel tight binding model with nodal sites L and R (on the left and right) connecting external current-carrying semi-infinite leads by hopping matrix elements $-\alpha_L$ (on the left) and $-\beta_R$ (on the right), and internal branches by hopping matrix elements $-\alpha_i$ and $-\beta_i$ (i =1, 2) respectively. The energies of the nodal sites are ε_L^0 and ε_R^0. The on-site energy and hopping matrix elements are ε_1 and $-\gamma_1$ for Channel 1, ε_2 and $-\gamma_2$ for Channel 2, and $\varepsilon_{L,R}$ and $-\gamma_{L,R}$ for leads L and R. All the on-site energies are set to 0, and $-\gamma_L = -\alpha_L = -\gamma_R = -\beta_R = -2$, $-\gamma_i = -1.5$, $-\alpha_i = -\beta_i = -0.01$, where i =1, 2.

(C) Transmission spectra for two- and single-channel molecules with two identical conducting channels.

(D) Conductance ratio (ρ) of the total conductance of cyclophane circuits (G_{II}) over the conductance of Channel 1 (G_I).

(E) Schematic illustration showing the coherent tunneling process across an asymmetric two-channel circuit with energy differences between its two channels. The blue and red colours indicate the phases of the frontier molecular orbitals. Here the ε_1 is shifted downwards by 0.3 eV compared with ε_2.

(F) Transmission spectra of the two-channel molecule (black) in (E) and its single-channel control molecules, namely Channel 1 (blue) and Channel 2 (red).

(G) Conductance ratio of the two-channel system over Channel 1 (blue), Channel 2 (red), and the average (black) of Channel 1 and 2, respectively.

(H) Schematic illustration showing a coherent tunneling process across an asymmetric two-channel circuit with phase differences between its two channels. The sign of $-\gamma_1$ is set opposite to that of

$-\gamma_2$, resulting in a phase exchange in HOMO–1 and LUMO orbitals. In this case, the new LUMO and LUMO+1 interfere constructively, while the HOMO and LUMO interfere destructively.

(I) Transmission spectra of the two-channel molecule (black) in (H) and its single-channel control molecules, namely Channel 1 (blue) and Channel 2 (red).

(J) Conductance ratio of the two-channel system over Channel 1 (blue), Channel 2 (red), and the average (black) of Channel 1 and 2, respectively. All the conductance is evaluated via $G = G_0 T(E_F)$.

When an electron tunnels (**Figure 1B**) through a non-interacting two-channel cyclophane circuit present in the same molecule represented by **Channel 1** shown in blue and **Channel 2** shown in red in **Figures 1A** and **2A**, QI takes place between the two channels. In order to appreciate the mechanism, a two-orbital Hückel tight-binding model can be utilized to describe each channel. Starting with two identical channels, CQI is observed[15,30] (**Figure 1C**) over the whole energy range in the HOMO-LUMO gap, as demonstrated by the higher transmission functions for two-channel systems, and specifically when a conductance ratio $\rho = G_{II} / G_I = 4$ is obtained (**Figure 1D**), revealing that the total conductance obeys the superposition law[29]

$$G = G_1 + G_2 + 2\sqrt{G_1 G_2} = 4\ G_1 \quad (1)$$

where G_{II} and G_I is the conductance of the two-channel target and single-channel control molecules, respectively. G_1 and G_2 is the effective conductance of each channel and $G_I = G_1 = G_2$ where these two channels are identical.

As reported previously[13,31-35] if the coupling between the molecule and electrode is weak, the effect of QI on charge transport can be predicted by examining Green's function $G(E)$ of the isolated molecule. The transmission amplitude of an electron with energy E from site i to j is proportional to $G_{i,j}(E)$, which can be expressed as

$$G_{i,j}(E) = \sum_{n=1}^{N} \frac{a_n}{E-\varepsilon_n} \quad (2)$$

In this expression, $a_n = \phi_i^n \phi_j^n$, where ϕ_i^n is the amplitude of n^{th} molecular orbital (MO) on site *i* and ε_n is the corresponding energy of the MO. In the case of our two-channel cyclophanes, charge transport is dominated by the LUMO product $a^L = \phi_i^L \phi_j^L$ and LUMO+1 product $a^{L+1} = \phi_i^{L+1} \phi_j^{L+1}$, where **equation (2)** can be re-written as

$$G_{i,j}(E) \approx \frac{a^L}{E-\varepsilon_L} + \frac{a^{L+1}}{E-\varepsilon_{L+1}} = \frac{1}{\Delta}\left(a_{\text{L}} + \frac{a_{\text{L+1}}}{\alpha}\right) \quad (3)$$

where ε_L and ε_{L+1} are the LUMO and LUMO+1 MO energies, $\Delta = E - \varepsilon_L$ and $\alpha = \frac{E-\varepsilon_{L+1}}{E-\varepsilon_L}$. When electrons of energy E less than ε_L propagate through two-channel cyclophanes, $\alpha > 1$. Therefore, for such sub-LUMO energies when a_L and a_{L+1} have the same sign, the term $\left(a_{\text{L}} + \frac{a_{\text{L+1}}}{\alpha}\right)$ in **equation (3)** is non-zero and CQI occurs. In contrast, when a_{L} and $a_{\text{L+1}}$ have opposite signs, $\left(a_{\text{L}} + \frac{a_{\text{L+1}}}{\alpha}\right)$ vanishes at a specific energy if $|a_{\text{L+1}}| > |a_L|$ and DQI will occur. In contrast, when *E* lies between the LUMO and LUMO+1, $\alpha < 0$. Therefore, for such supra-LUMO energies, **equation (3)** predicts that CQI occurs when a_L and a_{L+1} have opposite signs, while DQI occurs when a_{L} and $a_{\text{L+1}}$ have the same sign. This means that sub-LUMO CQI is accompanied by supra-LUMO DQI and vice versa.

In order to illustrate these QI features, an energy difference of two conducting channels is introduced by decreasing the on-site energy ε_2 of **Channel 2** to –0.3, while maintaining $\varepsilon_1 = 0$ for **Channel 1**. A graphical representation of the resulting frontier MOs is shown in **Figure 1E** with blue and red colours depicting different phases of the bonding and anti-bonding orbitals for the two weakly-coupled channels. According to **equation (3)**, sub-LUMO CQI is realized (**Figure 1F**, blue shaded region below and close to LUMO level) and a conductance ratio ρ of ~4 is obtained (**Figure 1g**, blue shaded region) and as expected, this is accompanied by supra-LUMO DQI (**Figures 1F** and **1G**, pink shaded region) between the LUMO and LUMO+1. In order to illustrate the opposite

case, a phase difference between the two channels is introduced by setting $-\gamma_1 = -1.5$ and $-\gamma_2 = +1.5$, leading to an exchange of the sub-LUMO QI features between LUMO and LUMO+1 (**Figure 1H**). In this case, sub-LUMO DQI is present (**Figures 1I** and **1J**, pink shaded region) in the two-channel cyclophanes, accompanied by supra-LUMO CQI, and therefore the conductances of the single-channel molecules are higher than those of the two-channel cyclophanes, resulting in a conductance ratio $\rho \ll 1$. These results demonstrate that the two-channel cyclophane circuits have the potential to provide a versatile platform for tuning room-temperature QI-mediated electron transport features.

RESULTS AND DISCUSSION

Preparation of Target and Control Compounds

In the case of the tetracationic cyclophanes[36] (**Figure 2A**), the electron withdrawing nature of the pyridinium unit facilitates the LUMO-dominated electron transport by lowering the energy of the LUMOs of each conducting branch towards the Au Fermi level (E_F), while pushing the HOMOs away from the E_F. On account of the convenience in their synthesis and the ease of functionalization, cyclophanes with different dimensions[37,38] and optoelectronic properties[39,40] can be prepared using a simple, two-step S_N2 reaction (**Scheme S1**) by choosing appropriate building blocks, namely extended viologens. By using[30] phenylene sulphide as the anchor groups, these cyclophanes can be incorporated into single-molecule circuits. Four methylene (-CH_2-) linkers break the conjugation between the anchor and the backbone, in a manner which weakens the coupling between the two channels and preserves the intrinsic LUMO-dominated transport properties of each conducting channel. These experiments demonstrate that the tetracationic cyclophane platform enables the construction of different electronic components[41-44] — namely, conductors and insulators — based on only one molecular platform.

The structural formulae of the two-channel tetracationic cyclophanes (***n*–D**•4PF_6, n = 1−6) and the single-channel control compounds (***n*–S**•2PF_6, n = 1−6) are shown in **Figure 2A** and **Scheme S1**. These cyclophanes — with one channel, an extended viologen unit[37] and the other channel, an identical or modified extended viologen unit, connected to common phenylene sulphide anchors at each end — can be synthesized in a straightforward two-step S_N2 reaction. In this way, the cyclophane circuits can be constructed easily by changing the extended viologen building blocks, thereby providing a versatile means of building a variety of cyclophane circuits. We demonstrate here that, by introducing energy differences or phase shifts into the two channels of the cyclophane circuits, the flow of electricity can be manipulated through the LUMO-mediated CQI or DQI, leading to extreme conductance promotion and suppression. Experimentally, the energy difference can be introduced by inserting *N*-substituted heterocycles between two pyridinium units. In contrast, the insertion of double (-HC=CH-) or triple (-C≡C-) bond into the conducting channel changes the phase of LUMOs. Detailed synthetic protocols and characterizations are provided in the **Supplementary Information** (**Figures S1–S30**). Further atomic-level structural information was obtained (**Figures S31–S35**) from single-crystal X-ray diffraction analyses, which reveal unambiguously the conformations of the cyclophane analogs in the solid state. All these analogs adopt (**Figure S36**) an extended hexagonal geometry with average dimensions of 20.9 × 9.9 Å (length × width).

The electron withdrawing pyridinium units lower the LUMOs of each conducting channel to the Au Fermi level. In an attempt to obtain the energy level alignments of each conducting channel, we performed UV−Vis absorption spectroscopy (**Figure S37**), cyclic voltammetry (**Figure S38**), and density functional theory (DFT) calculations. In order to avoid overlaps in either their absorption peaks or in the redox potentials of the two backbones in a particular cyclophane, we performed the experiments on model compounds — namely, ***n*–Me**•2PF_6 (n = 1−6), having the same backbones, but terminated with methyl groups at both ends. The energy-level diagrams

(**Figure 2B, Figure S39** and **Table S1**) of the six channels (n = 1−6) demonstrate that the HOMOs are below –7.0 eV, while the LUMOs are around –4.0 eV, both values being close to that (~ –5.0 eV) of Au Fermi level, emphasizing that electron transport through these channels is LUMO-dominated. In the case of two-channel cyclophanes, DFT-calculated distributions of frontier MOs (**Figure S46**) of **4–D**$^{4+}$ reveal that HOMO and HOMO–1 are localized on the phenylene sulphide anchors of the cyclophane and therefore do not contribute significantly to electron transport, while the LUMO and LUMO+1 are highly delocalized across the backbone. Thus, we expect transport in ***n*–D**$^{4+}$ will be dominated by the delocalized LUMO channels where the HOMOs are effectively absent.

Single-Molecule Conductance Measurement

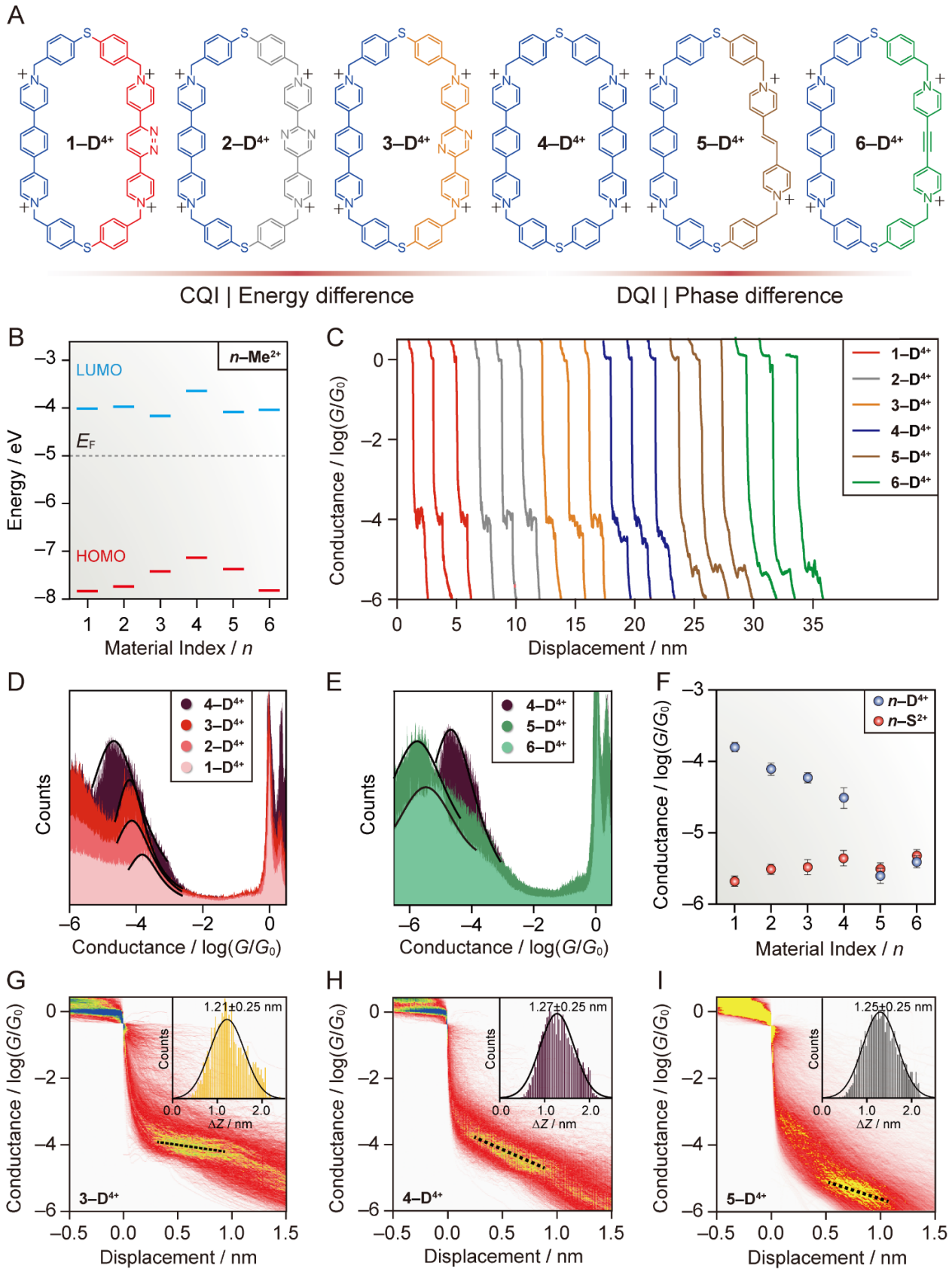

Figure 2. | Single-Molecule Conductance of the Cyclophane Circuits

(A) Structural formulae of ***n*–D^{4+}** (*n* = 1−6).

(B) Energy level diagram for ***n*–Me^{2+}** (*n* = 1−6) constructed from experimental data.

(C) Examples of conductance versus displacement traces measured with ***n*–D^{4+}** (*n* = 1−6). The traces are shifted horizontally for the sake of clarity.

(D and E) 1D conductance histograms generated from ~5,000 traces for cyclophanes with *N*-substituted backbones (D) and carbon-carbon double or triple bond-inserted backbones (E).

(F) Summary of the conductance results obtained from two-channel cyclophanes ***n*–D^{4+}** (*n* = 1–6) (blue) and their single-channel control compounds ***n*–S^{2+}** (*n* = 1–6) (red).

(G–I) 2D conductance-displacement histograms for **3–D^{4+}** (G), **4–D^{4+}** (H), and **5–D^{4+}** (I), respectively. Insets show the stretching distance distribution for each molecule obtained from the conductance region.

We measured the single-molecule conductance of the cyclophane junctions using a scanning tunneling microscope-based break junction[45,46] (STM-BJ) technique as described in the **Methods** section and **Supplementary Section G** (**Figures S40–S42**). **Figure 2C** shows typical single-molecule breaking traces for the six cyclophane junctions — namely ***n*–D^{4+}** (*n* = 1−6). Clear conductance plateaus, which are located ranging from $10^{-3.8}$ to $10^{-5.6}$ G_0, can be attributed to the conductance signature of each molecule. We compiled ~5,000 traces into logarithmically binned one-dimensional (1D) and two-dimensional (2D) conductance histograms without data selection. **Figures 2D** and **2E** display the 1D conductance histograms for the cyclophanes with *N*-substituted derivatives (**1–D^{4+}**, **2–D^{4+}** and **3–D^{4+}**), in addition to double (**5–D^{4+}**) and triple (**6–D^{4+}**) bond inserted backbones, respectively, using the symmetric cyclophane (**4–D^{4+}**) as a benchmark. Quantitatively, we obtain (**Figure 2F** and **Table S2**) the most probable conductance values by fitting a Gaussian function. In good agreement with the theoretical predications (**Figure 1**), the conductances ($10^{-3.82}$ to $10^{-4.21}$ G_0) of the *N*-substituted asymmetric cyclophanes (**1–D^{4+}**, **2–D^{4+}** and

3–D^{4+}) differ in so far as they are ~5 times higher than the value ($10^{-4.50}$ G_0) for the symmetric cyclophane **4–D^{4+}**. While double/triple bond-inserted cyclophanes (**5–D^{4+}** and **6–D^{4+}**) show suppressed conductances ($10^{-5.62}$ and $10^{-5.32}$ G_0) by up to one order of magnitude lower than that of **4–D^{4+}**. The corresponding 2D conductance-displacement histograms allow an intuitive determination of the conductance distribution and the junction elongation. By comparing the 2D histograms across the series of the two-channel cyclophanes, we note that **3–D^{4+}** exhibits (**Figure 2G**) a rather high and flat 2D conductance histogram, while there is a pronounced slope in the case of **4–D^{4+}** (**Figure 2H**) and **5–D^{4+}** (**Figure 2I**). The observed junction elongation — obtained by the stretching distance adding (**Figures 2G–2I**, insets) to ~0.6 nm Au snapping back distance[47] — corresponds well with the molecular length, i.e., ~2.0 nm as summarized in **Figure S36**. Using **4–D^{4+}** as a benchmark, we have reached the conclusion that **1–D^{4+}**, **2–D^{4}** and **3–D^{4+}** are single-molecule conductors, while **5–D^{4+}** and **6–D^{4+}** are single-molecule insulators, despite the fact that these cyclophanes share similar conformations and tunneling distances.

In order to confirm the LUMO-dominated electron transport mechanism, we carried out thermoelectric experiments. The experimental details in present in **Supplementary Section G** (**Figure S43**). We explored (**Figure S43A**) the thermopower nature of **5–D^{4+}** and determined (**Figure S43B**) its Seebeck coefficient (S) of –52.53±3.97 μV K^{-1}. The negative value of S reveals that the LUMO of **5–D^{4+}** is closer to the Fermi level of Au electrodes. Nevertheless, the large value of S indicates a steep slope near Au Fermi level in the transmission curve of **5–D^{4+}** (**Figure 3A**).

DFT-Based Theoretical Analysis

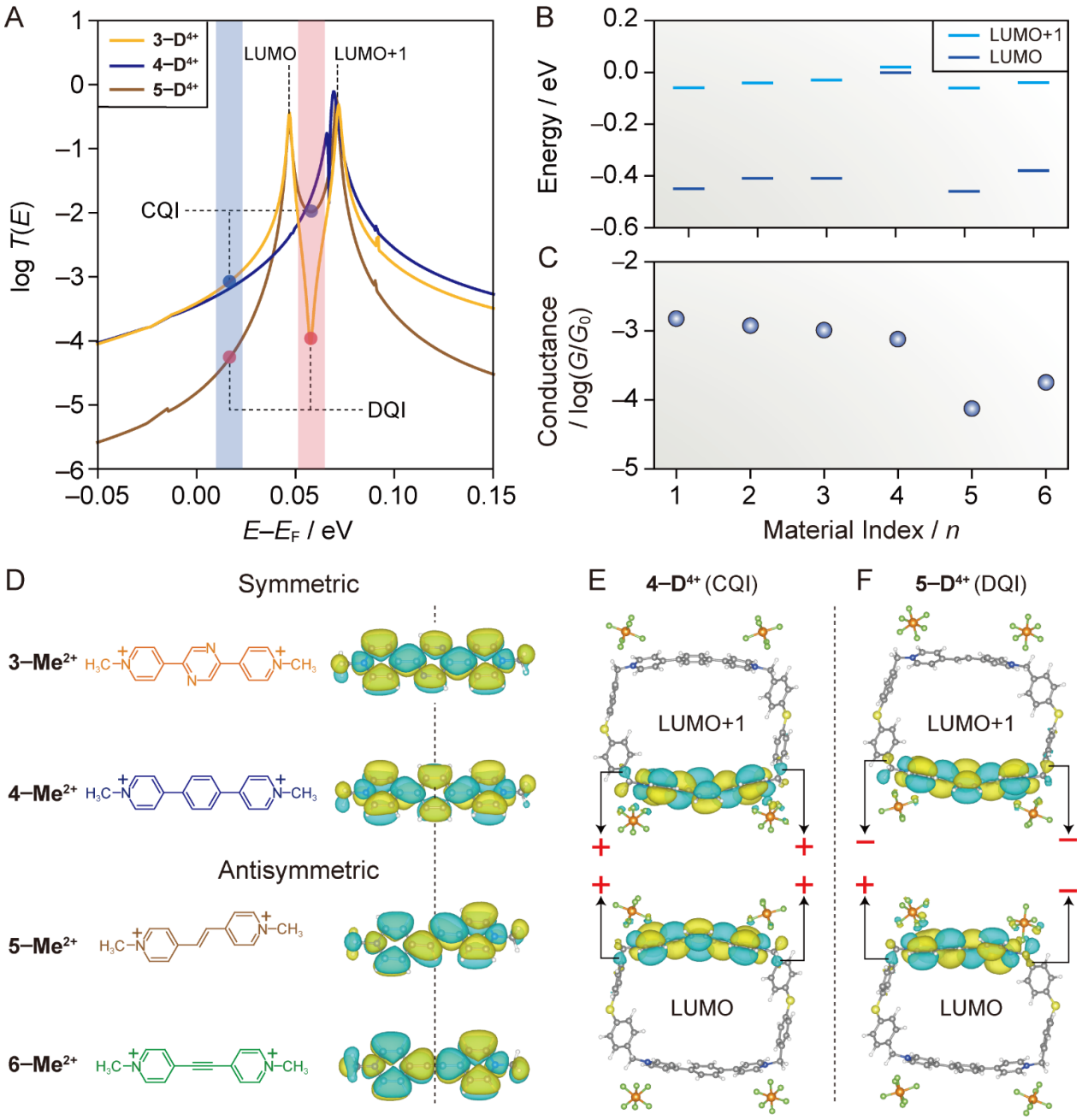

Figure 3. | Transport properties for two-channel cyclophanes

(A) Transmission functions of **3–D**$^{4+}$ (yellow), **4–D**$^{4+}$ (blue), and **5–D**$^{4+}$ (grey) calculated using DFT. DQI and CQI features are denoted by dashed lines.

(B) DFT-Calculated LUMO (dark blue) and LUMO+1(light blue) energy levels for ***n*–D**$^{4+}$ ($n = 1-6$ is the material index). LUMO of **4–D**$^{4+}$ is used as a reference.

(C) DFT-Calculated conductances evaluated at $E_F - E_F^{DFT} = 0.02\ eV$ for ***n*–D**$^{4+}$.

(D) The LUMOs for the backbone molecules ***n*–Me^{2+}** where the vertical dashed black line is utilized to distinguish their different symmetric properties.

(E and F) Wavefunctions of the LUMO and LUMO+1 for **4–D^{4+}** (E) and **5–D^{4+}** (F) where '+', '–' (marked in red) are used to distinguish the phases of their wavefunctions.

In order to gain further insight into the conductance evolution within the family of asymmetric tetracationic cyclophanes, we calculated the transmission functions, $T(E)$, by combining the DFT package SIESTA[48] with the quantum transport code Gollum[49]. See **Methods** and **Supplementary Section H** for details of these calculations. For estimating the electronic conductance, we attach molecules to Au electrodes. The optimum distance between Au tip and S is found to be 2.4 Å with a binding energy of 0.75 eV (**Figure S47**). The DFT-predicted Au Fermi level is located (**Figure 3A** and **Figure S48**) close to the LUMO peaks of the positively charged conducting channels. In the case of the symmetric cyclophane **4–D^{4+}**, there are no resonances caused by the HOMO–1 and HOMO in the transmission function (**Figure S48**). Such a LUMO-dominated electron transport mechanism is applicable for all two-channel cyclophanes (***n*–D^{4+}**, n = 1–6) under investigation and is mediated by the delocalized nature of the LUMOs along the separate channels. The DFT-predicted energy level diagrams of the isolated cyclophanes (**Figure 3B**) show that the LUMO and LUMO+1 of the symmetric cyclophane **4–D^{4+}** are almost degenerate. By contrast, this degeneracy is lifted in the asymmetric cyclophanes, **1–D^{4+}**, **2–D^{4+}** **3–D^{4+}**, **5–D^{4+}** and **6–D^{4+}**, leading to a decrease in the LUMO energy by ~0.40 eV, compared with the LUMO of the **4–D^{4+}**.

The LUMO/LUMO+1 energy difference in the asymmetric cyclophanes, indicated by their transport resonances (**Figure 3A**), shrinks to ~0.02 eV, because of the rearrangement of energy levels imposed by their interactions with Au electrodes. As the LUMOs shift towards the Au Fermi level, the corresponding conductance increases slightly from $10^{-3.12}$ G_0 for **4–D^{4+}** to ~$10^{-2.99}$ G_0 and $10^{-2.92}$ G_0 for **3–D^{4+}** and **2–D^{4+}**, respectively, and then undergoes further increases (**Figure 3C**) to $10^{-2.82}$ G_0 for **1–D^{4+}**. By contrast, the single-molecule conductance of **5–D^{4+}** and **6–D^{4+}** decreases

(**Figure 3C**) to $10^{-4.12}$ and $10^{-3.74}$ G_0, respectively. This theoretically predicted trend agrees well with the experimentally measured results (**Figure 2F**).

In an attempt to shed light on the opposite conductance trends obtained in *N*-substituted derivatives (**1–D**$^{4+}$, **2–D**$^{4+}$ and **3–D**$^{4+}$) and double/triple bond-inserted (**5–D**$^{4+}$ and **6–D**$^{4+}$) backbones, we analyzed the phase patterns of their MOs. The phase symmetries (**Figure 3d**) are determined from the LUMOs of the isolated channels. When the phenylene ring of **4–Me**$^{4+}$ is substituted by two N atoms (**3–Me**$^{2+}$), the symmetry does not change, as indicated by the vertical black dashed line in **Figure 3D**. When the phenylene ring is replaced by a carbon-carbon double (-CH=CH-) (**5–Me**$^{2+}$) or triple (-C≡C-) bond (**6–Me**$^{2+}$), the symmetric LUMO becomes antisymmetric. These separated channels are then assembled to afford two-channel cyclophane circuits. In the case of **4–D**$^{4+}$ (**Figure 3E**), the LUMO and LUMO+1 are symmetric, with the same phase alterations along their LUMOs, and therefore both a_{L} and $a_{\mathrm{L+1}}$ in **equation (3)** are positive, as indicated by the "+" sign at both ends of the two branches of **4–D**$^{4+}$. This situation results in CQI (**Figure 3A**, blue curve) at energies below the LUMO. In contrast, for **5–D**$^{4+}$ (**Figure 3F**), the LUMO+1 is symmetric leading to a positive $a_{\mathrm{L+1}}$. The LUMO channel, however, is antisymmetric, as indicated by the "+" sign at one end and "–" sign at the other end of **5–D**$^{4+}$, leading to a negative a_{L}. As a result, sub-LUMO DQI occurs (**Figure 3A**, grey curve) at energies below the LUMO and supra-LUMO CQI occurs in the LUMO/LUMO+1 gap for **5–D**$^{4+}$. Considering the fact that the E_{F} lies below the LUMOs, the conductance of **3–D**$^{4+}$ and **4–D**$^{4+}$ can be predicted (**Figure 3A**) to be much higher than the value obtained for **5–D**$^{4+}$, which is in good agreement with the experimental results.

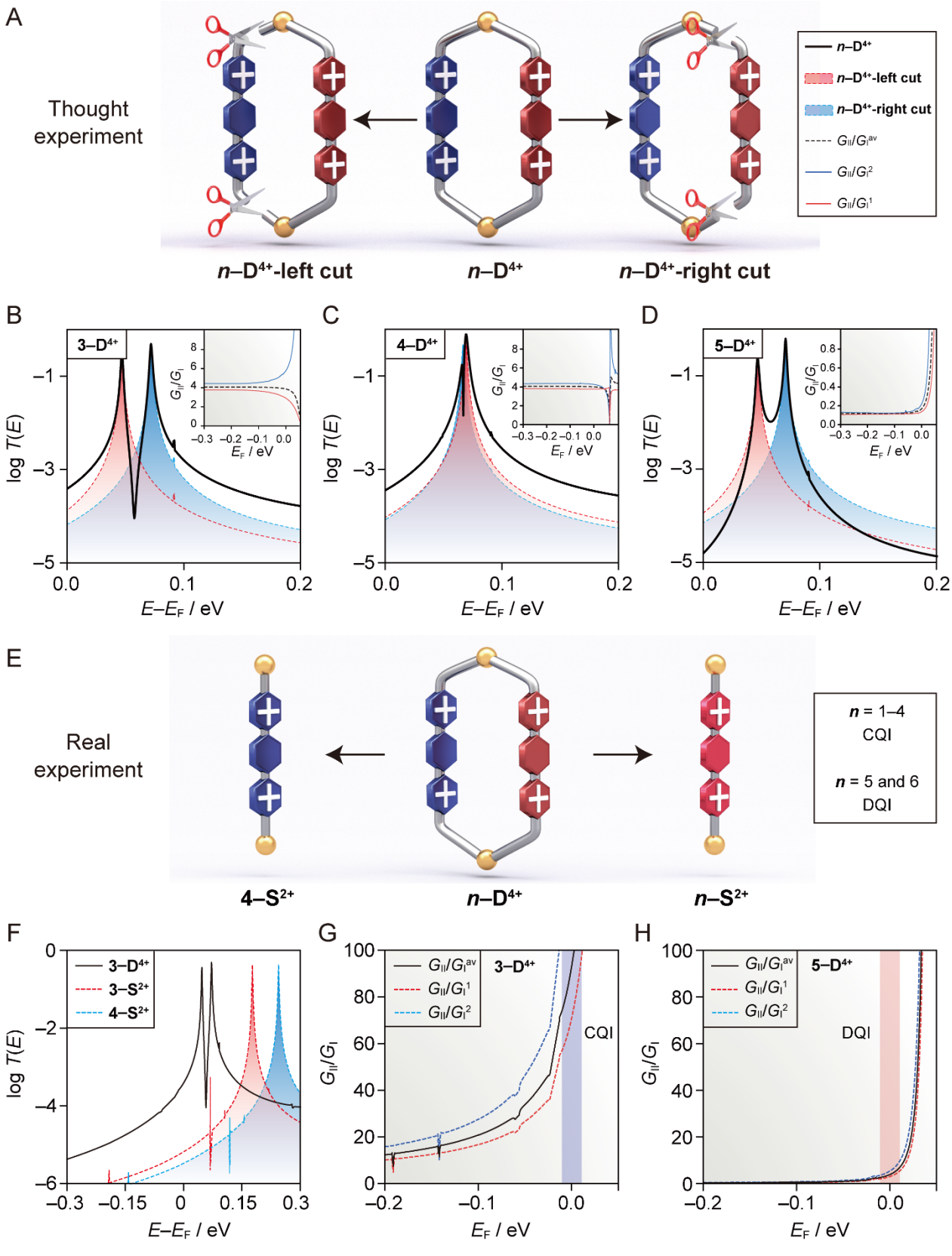

Figure 4. | Transport properties for two-channel and one-channel compounds

(A) Schematic illustration showing a thought experiment for obtaining single-channel control compounds for ***n*–D^{4+}** — namely, ***n*–D^{4+}-left cut** (left) and ***n*–D^{4+}-right cut** (right), obtained by cutting the coupling as a result of modifying the Hamiltonian manually.

(B–D) Transmission spectra (black) for **3–D^{4+}** (B), **4–D^{4+}** (C), and **5–D^{4+}** (D) and the corresponding artificial single-channel control molecules. ***n*–D^{4+}-left cut** is shown in red and ***n*–D^{4+}-right-cut** is shown in blue. Insets of (B–D) show the conductance ratio (ρ = G_{II} / G_I) of two-channel cyclophanes over single-channel control molecules. The value of ρ depends on whether G_I is chosen to be the conductance of the left-cut (red curve), the right-cut (blue curve), or the average (black curve) of the two control molecules.

(E) Schematic illustration showing the real experiment for obtaining single-channel control molecules of ***n*–D^{4+}** — namely, **4–S^{2+}** (left) and ***n*–S^{4+}** (right), obtained from synthesis.

(F) Transmission spectra for **3–D^{4+}** (black) and its two single-channel controls — namely **3–S^{2+}** (red) and **4–S^{2+}** (blue).

(G and H) Conductance ratio of **3–D^{4+}** and **5–D^{4+}** showing clear CQI and DQI signatures, respectively, along with the inter-channel gating effect.

Quantitatively, the effect of QI can be examined by extracting the conductance ratio, $\rho = G_{II} / G_I$. The conductance of the single-channel control molecule, G_I, is obtained in two different ways. First, a thought experiment is performed (**Figure 4A**) in which two artificial molecules— namely, ***n*–D^{4+}-left cut** and ***n*–D^{4+}-right cut** — are obtained by cutting the cyclophanes by scissors. This severing process decouples the part between the scissors from the remaining part of the molecule by setting the Hamiltonian matrix elements to zero (**Figure S49**), thereby creating a single-channel conducting wire without changing the electrostatic environment. In the case of **3–D^{4+}** (**Figure 4B**, red curve) and **4–D^{4+}** (**Figure 4C**, red curve), the severing experiments decrease the transmission coefficients below the LUMO, because sub-LUMO CQI in this region has been removed. As a result, the electrical conductances of the two-channel cyclophanes are much higher (ρ = ~4) (insets

of **Figure 4B,C**) than their artificial single-channel control molecules. In contrast, the severing experiment increases (**Figure 4D,** red curve) the transmission coefficients of **5–D**$^{4+}$ below the LUMO on account of the removal of sub-LUMO DQI in this energy region. As a result, the conductance of the two-channel cyclophane is suppressed (ρ = ~0.1) compared with that of the artificial single-channel control molecules. The extreme promotion or suppression of single-molecule conductance, caused by different QI behaviour, also applies (**Figure S50**) to other cyclophanes. Consequently, for the energy region below LUMO, ρ is ~4 for **1–D**$^{4+}$ and **2–D**$^{4+}$ owing to CQI, whereas the value decreases to ~0.1 for **6–D**$^{4+}$ on account of phase difference-induced DQI.

The second way to obtain transmission curves is based on the synthetically realisable single-channel control molecules — namely, ***n*–S**$^{2+}$ (n = 1–6) (**Figure 4E**). On comparing (**Figure 4F**) the transmission curves of **3–D**$^{4+}$ (**Figure 4F**, black curve) and **3–S**$^{2+}$ (**Figure 4F**, red curve) in the sub-LUMO region, we observed similar decreasing trends in the transmission coefficients for single-channel control molecules. The LUMO transmission resonances of **3–S**$^{2+}$ were shifted upwards in energy for the simple reason that the electrostatic environment has been changed by removing one of the dicationic channels. The strong electrostatic interactions between charged parallel channels, however, serve as a chemical gate to promote[30] the effective conductance of each channel. In the case of **3–D**$^{4+}$ (**Figure 4F**), the energy level shift of LUMOs increases the conductance of the two-channel cyclophane near the Au Fermi energy, leading to a total conductance promotion of ~60 (**Figure 4G**), a value much higher than ~4 caused by CQI (**Figure 4B**). Such a promotion in total conductance, which originates from a combination of CQI and inter-channel gating is also obtained (**Figure S51**) for **1–D**$^{4+}$, **2–D**$^{4+}$ and **4–D**$^{4+}$, while the extreme suppression of conductance — with a small ρ of ~2 obtained for **5–D**$^{4+}$ (**Figure 4H**) and ~10 for **6–D**$^{4+}$ (**Figure S52**) — can be attributed to the DQI feature. The interchannel gating effect has also been verified (**Figure S43**) by flicker noise measurement which demonstrated that the noise power

scales as ~$G^{2.0}$, indicating a strong through-space Columbic interaction between these two positively charged conducting channels. Despite the unknown features of our experiments — such as (i) the conformations of the molecules, (ii) the atomic-scale contact details between the electrodes and anchors, and (iii) the interchannel gating efficiencies — these predicted qualitative features agree well with the experimental trends — namely, CQI (**1–D**$^{4+}$, **2–D**$^{4+}$, **3–D**$^{4+}$ and **4–D**$^{4+}$) gives high conductances, while DQI (**5–D**$^{4+}$ and **6–D**$^{4+}$) leads to low values.

Conclusion

We have demonstrated the ability to control the flow of electricity through two-channel cyclophanes by introducing energy and phase shifts into the de Broglie waves of electrons traversing different pathways. DFT calculations, combined with quantum transport theory, demonstrate that the family of tetracationic cyclophanes provides an ideal platform for exploring and tuning room-temperature sub-LUMO and supra-LUMO quantum interference-mediated electron transport. Their electrical conductance is controlled by quantum interference between their LUMO and LUMO+1, whereas their HOMOs play no significant role. By making the electron transport through each conducting channel LUMO-dominated, the switching between the constructive and destructive quantum interferences can be simply manipulated by changing one of the two conducting channels. Our research demonstrates a modular design of intramolecular circuits, which enables the construction of fundamental building elements for single-molecule electronics, namely, conductors and insulators. The design is based on a single tetracationic cyclophane platform and opens the way to new design strategies for single-molecule electronic devices.

EXPERIMENTAL PROCEDURES

Resource Availability

Lead Contact

Further information and requests for resources and reagents should be directed to and will be honored by the Lead Contact, Professor J. Fraser Stoddart (stoddart@northwestern.edu).

Materials Availability

This study did not generate new unique reagents.

Data and Code Availability

The data that support the findings of this investigation are available from the corresponding authors upon reasonable request. All single-crystal data have been deposited on the Cambridge Crystallographic Data Centre (CCDC) and can be downloaded free of charge from www.ccdc.cam.ac.uk/data_request/cif. The reference numbers of the **1–D**$^{4+}$, 2**–D**$^{4+}$, 3**–D**$^{4+}$, 4**–D**$^{4+}$ and **5–D**$^{4+}$ are CCDC: 2074920, 2074921, 2074922, 1954282 and 2035271, respectively.

Materials

The tetracationic cyclophanes were prepared — with 1,1′-thiobis[4-(bromomethyl)benzene] and extend bipyridine as the starting materials — by a sequence of two-step S_N2 reactions in MeCN at 80 °C. Details of the synthesis and characterization can be found in the **Supplemental Sections A–D**, **Schemes S1–S17** and **Figures S1–S36**.

STM-BJ Measurements

The single-molecule conductance measurements were performed using the STM-BJ technique with a home-built setup housed in a plastic glovebox filled with N_2 at 298 K as described in a previous report[47]. Single-molecule junctions were created by repeatedly forming and breaking an Au point contact in a MeCN (Sigma–Aldrich, 99% purity) solution of the cyclophanes with a bias of 100 mV. An electrochemically etched Au wire (Ø = 0.25 mm, 99.999% purity, Alfa Aesar) was coated and was used as the tip. The Au substrates, which were prepared by the evaporation of ~100 nm Au (99.999% purity, Alfa Aesar) at ~1 Å/s onto silicon substrates, were cleaned with a Piranha solution before carrying out the experiments. In order to suppress the background current from

MeCN, we coated[50] a thin layer of Apiezon® wax onto the Au tip apex. Single-molecule conductance was measured using the STM–BJ technique[45-47] under ambient conditions in MeCN solutions containing 0.1 mM cyclophanes. Thousands of traces were collected and are presented in the form of conductance histograms without data selection. Accordingly, the peaks corresponded to the most frequently observed conductance values. Further details are provided in **Supplemental Section G**.

DFT Simulations

Geometrical optimizations were performed by using the DFT code SIESTA[48], with (i) a local density approximation LDA functional, (ii) a double-ζ basis for Au, (iii) a double-ζ polarized basis for other elements, (iv) a cutoff energy of 200 Ry and (V) a 0.05 eV/Å force tolerance. In order compute their electrical conductance, the molecules were each placed between pyramidal Au electrodes. For each molecule, the transmission coefficient, $T(E)$, describing the propagation of electrons of energy E from left to right electrodes was calculated using Gollum code[49], which combines the mean-field Hamiltonian and overlap matrices of the DFT code SIESTA with Landauer-based quantum transport theory using the expression

$$T(E) = \mathrm{Tr}\left[\Gamma_L(E) G_r(E) \Gamma_{\mathrm{R}}(E) G_r^{\dagger}(E)\right]$$

where $\Gamma_{\mathrm{L,R}}(E) = \frac{\mathrm{i}\left(\Sigma_{\mathrm{L,R}}(E) - \Sigma_{\mathrm{L,R}}{}^{\dagger}(E)\right)}{2}$, $G_r(E) = (g^{-1} - \Sigma_{\mathrm{L}} - \Sigma_{\mathrm{R}})^{-1}$, g is the Green's function of the isolated molecule. $\Gamma_{\mathrm{L,R}}$ determines the widths of transmission resonances, $\Sigma_{\mathrm{L,R}}(E)$ are the self-energies describing the contact between the molecule and left (L) and right (R) electrodes, while G_r is the retarded Green's function of the molecule in the presence of the electrodes. The low temperature conductance was extracted from the transmission spectrum and evaluated employing the following formulae: $G = G_0 T(E_{\mathrm{F}})$, where $G_0 = \frac{2e^2}{h}$ is the conductance quantum, h is the Planck's constant, e is the charge on a proton and E_{F} is the Fermi energy.

SUPPLEMENTAL INFORMATION

Supplemental Information can be found online at https://doi.org/10.1016/j.matt.xxxx.

Acknowledgements

The authors thank Northwestern University (NU) for its continued support of this research. The authors also acknowledge the Integrated Molecular Structure Education and Research Center (IMSERC) at NU for providing access to equipment for the experiments. The research work in Xiamen University was supported by the National Key R&D Program of China (2017YFA0204902) and the National Natural Science Foundation of China (Grants 21673195 and 21722305). Computational investigations were supported by the United Kingdom Engineering and Physical Sciences Research Council (EPSRC) through grant no. EP/N017188/1, EP/M014452/1, EP/P027156/1, and EP/N03337X/1. Support from the European Commission, European Union, was provided by the FET Open project 767187 – QuIET.

Author contributions

H.C. and J.F.S. conceived the idea and designed the experiments. H.C. and S. H. wrote the manuscript with inputs from all authors. H.C. performed most of the experiments including syntheses, characterizations, measurements and data analyses. H.C., F.J. and P.Z. carried out the break junction experiments. L.Z., Y.J. and B.S., assisted with synthesis and characterization of cyclophanes. S.H., Q.W. and C.J.L. developed the underlying theoretical concepts, including the idea of using double and triple bonds to tune the QI between the two branches. H.C., W.H., C.J.L., and J.F.S. co-supervised the project. All authors contributed to and commented on the contents of manuscript.

DECLARATION OF INTERESTS

The authors declare no competing interests.

REFERENCES

1 Joachim, C., Gimzewski, J. K. and Aviram, A. (2000) Electronics using hybrid-molecular and mono-molecular devices. Nature *408*, 541–548.

2 Nitzan, A. and Ratner, M. A. (2003) Electron transport in molecular wire junctions. Science *300*, 1384–1389.

3 Flood, A. H., Stoddart, J. F., Steuerman, D. W. and Heath, J. R. (2004) Whence molecular electronics? Science *306*, 2055–2056.

4 Xiang, D., Wang, X., Jia, C., Lee, T. and Guo, X. (2016) Molecular-scale electronics: From concept to function. Chem. Rev. *116*, 4318–4440.

5 Su, T. A., Neupane, M., Steigerwald, M. L., Venkataraman, L. and Nuckolls, C. (2016) Chemical principles of single-molecule electronics. Nat. Rev. Mater. *1*, 16002.

6 Xin, N., Guan, J., Zhou, C., Chen, X., Gu, C., Li, Y., Ratner, M. A., Nitzan, A., Stoddart, J. F. and Guo, X. (2019) Concepts in the design and engineering of single-molecule electronic devices. Nat. Rev. Phys. *1*, 211–230.

7 Gehring, P., Thijssen, J. M. and van der Zant, H. S. J. (2019) Single-molecule quantum-transport phenomena in break junctions. Nat. Rev. Phys. *1*, 381–396.

8 Chen, H. and Stoddart, J. F. (2021) From molecular to supramolecular electronics. Nat. Rev. Mater. *6*, 10.1038/s41578-41021-00302-41572.

9 Cardamone, D. M., Stafford, C. A. and Mazumdar, S. (2006) Controlling quantum transport through a single molecule. Nano Lett. *6*, 2422–2426.

10 Yoshizawa, K., Tada, T. and Staykov, A. (2008) Orbital views of the electron transport in molecular devices. J. Am. Chem. Soc. *130*, 9406–9413.

11 Solomon, G. C., Andrews, D. Q., Hansen, T., Goldsmith, R. H., Wasielewski, M. R., Duyne, R. P. V. and Ratner, M. A. (2008) Understanding quantum interference in coherent molecular conduction. J. Chem. Phys. *129*, 054701.

12 Andrews, D. Q., Solomon, G. C., Van Duyne, R. P. and Ratner, M. A. (2008) Single molecule electronics: Increasing dynamic range and switching speed using cross-conjugated species. J. Am. Chem. Soc. *130*, 17309–17319.

13 Markussen, T., Stadler, R. and Thygesen, K. S. (2010) The relation between structure and quantum interference in single molecule junctions. Nano Lett. *10*, 4260–4265.

14 Guédon, C. M., Valkenier, H., Markussen, T., Thygesen, K. S., Hummelen, J. C. and van der Molen, S. J. (2012) Observation of quantum interference in molecular charge transport. Nat. Nanotechnol. *7*, 305–309.

15 Vazquez, H., Skouta, R., Schneebeli, S., Kamenetska, M., Breslow, R., Venkataraman, L. and Hybertsen, M. S. (2012) Probing the conductance superposition law in single-molecule circuits with parallel paths. Nat. Nanotechnol. *7*, 663–667.

16 Greenwald, J. E., Cameron, J., Findlay, N. J., Fu, T., Gunasekaran, S., Skabara, P. J. and Venkataraman, L. (2021) Highly nonlinear transport across single-molecule junctions via destructive quantum interference. Nat. Nanotechnol. *16*, 313–317.

17 Büttiker, M., Imry, Y. and Azbel, M. Y. (1984) Quantum oscillations in one-dimensional normal-metal rings. Phys. Rev. A *30*, 1982–1989.

18 Webb, R. A., Washburn, S., Umbach, C. P. and Laibowitz, R. B. (1985) Observation of *h/e* Aharonov-Bohm oscillations in normal-metal rings. Phys. Rev. Lett. *54*, 2696–2699.

19 Sautet, P. and Joachim, C. (1988) Electronic interference produced by a benzene embedded in a polyacetylene chain. Chem. Phys. Lett. *153*, 511–516.

20 Marvaud, V., Launay, J.-P. and Joachim, C. (1993) Electron transfer through 2,7,9,10-tetraazaphenanthrene: A quantum “interference” effect? Chem. Phys. *177*, 23–30.

21 Walter, D., Neuhauser, D. and Baer, R. (2004) Quantum interference in polycyclic hydrocarbon molecular wires. Chem. Phys. *299*, 139–145.

22 Ernzerhof, M., Zhuang, M. and Rocheleau, P. (2005) Side-chain effects in molecular electronic devices. J. Chem. Phys. *123*, 134704.

23 Papadopoulos, T. A., Grace, I. M. and Lambert, C. J. (2006) Control of electron transport through Fano resonances in molecular wires. Phys. Rev. B *74*, 193306.

24 Hong, W., Valkenier, H., Mészáros, G., Manrique, D. Z., Mishchenko, A., Putz, A., García, P. M., Lambert, C. J., Hummelen, J. C. and Wandlowski, T. (2011) An MCBJ case study: The influence of π-conjugation on the single-molecule conductance at a solid/liquid interface. Beilstein J. Nanotechnol. *2*, 699–713.

25 Kaliginedi, V., Moreno-García, P., Valkenier, H., Hong, W., García-Suárez, V. M., Buiter, P., Otten, J. L. H., Hummelen, J. C., Lambert, C. J. and Wandlowski, T. (2012) Correlations between molecular structure and single-junction conductance: A case study with oligo(phenylene-ethynylene)-type wires. J. Am. Chem. Soc. *134*, 5262–5275.

26 Baer, R. and Neuhauser, D. (2002) Phase coherent electronics: A molecular switch based on quantum interference. J. Am. Chem. Soc. *124*, 4200–4201.

27 Baer, R. and Neuhauser, D. (2002) Anti-coherence based molecular electronics: XOR-gate response. Chem. Phys. *281*, 353–362.

28 Liu, C., Walter, D., Neuhauser, D. and Baer, R. (2003) Molecular recognition and conductance in crown ethers. J. Am. Chem. Soc. *125*, 13936–13937.

29 Magoga, M. and Joachim, C. (1999) Conductance of molecular wires connected or bonded in parallel. Phys. Rev. B *59*, 16011–16021.

30 Chen, H., Zheng, H., Hu, C., Cai, K., Jiao, Y., Zhang, L., Jiang, F., Roy, I., Qiu, Y., Shen, D. et al. (2020) Giant conductance enhancement of intramolecular circuits through interchannel gating. Matter *2*, 378–389.

31 Lambert, C. J. *Quantum transport in nanostructures and molecules*. (IOP Publishing, 2021).

32 Markussen, T., Stadler, R. and Thygesen, K. S. (2011) Graphical prediction of quantum interference-induced transmission nodes in functionalized organic molecules. Phys. Chem. Chem. Phys. *13*, 14311–14317.

33 Yoshizawa, K. (2012) An orbital rule for electron transport in molecules. Acc. Chem. Res. *45*, 1612–1621.

34 Lambert, C. J. and Liu, S.-X. (2018) A magic ratio rule for beginners: A chemist's guide to quantum interference in molecules. Chem. Eur. J. *24*, 4193–4201.

35 Zheng, H., Hou, S., Xin, C., Wu, Q., Jiang, F., Tan, Z., Zhou, X., Lin, L., He, W., Li, Q. et al. (2019) Room-temperature quantum interference in single perovskite quantum dot junctions. Nat. Commun. *10*, 5458.

36 Dale, E. J., Vermeulen, N. A., Juríček, M., Barnes, J. C., Young, R. M., Wasielewski, M. R. and Stoddart, J. F. (2016) Supramolecular explorations: Exhibiting the extent of extended cationic cyclophanes. Acc. Chem. Res. *49*, 262–273.

37 Barnes, J. C., Juríček, M., Strutt, N. L., Frasconi, M., Sampath, S., Giesener, M. A., McGrier, P. L., Bruns, C. J., Stern, C. L., Sarjeant, A. A. et al. (2013) ExBox: A polycyclic aromatic hydrocarbon scavenger. J. Am. Chem. Soc. *135*, 183–192.

38 Juríček, M., Barnes, J. C., Dale, E. J., Liu, W.-G., Strutt, N. L., Bruns, C. J., Vermeulen, N. A., Ghooray, K. C., Sarjeant, A. A., Stern, C. L. et al. (2013) Ex2Box: Interdependent modes of binding in a two-nanometer-long synthetic receptor. J. Am. Chem. Soc. *135*, 12736–12746.

39 Gong, X., Young, R. M., Hartlieb, K. J., Miller, C., Wu, Y., Xiao, H., Li, P., Hafezi, N., Zhou, J., Ma, L. et al. (2017) Intramolecular energy and electron transfer within a diazaperopyrenium-based cyclophane. J. Am. Chem. Soc. *139*, 4107–4116.

40 Guo, Q.-H., Zhou, J., Mao, H., Qiu, Y., Nguyen, M. T., Feng, Y., Liang, J., Shen, D., Li, P., Liu, Z. et al. (2020) TetrazineBox: A structurally transformative toolbox. J. Am. Chem. Soc. *142*, 5419–5428.

41 Haiss, W., Wang, C., Grace, I., Batsanov, A. S., Schiffrin, D. J., Higgins, S. J., Bryce, M. R., Lambert, C. J. and Nichols, R. J. (2006) Precision control of single-molecule electrical junctions. Nat. Mater. *5*, 995–1002.

42 Sedghi, G., García-Suárez, V. M., Esdaile, L. J., Anderson, H. L., Lambert, C. J., Martín, S., Bethell, D., Higgins, S. J., Elliott, M., Bennett, N. et al. (2011) Long-range electron tunnelling in oligo-porphyrin molecular wires. Nat. Nanotechnol. *6*, 517–523.

43 Qiu, X. and Chiechi, R. C. (2020) Large-area molecular junctions: Synthesizing integrated circuits for next-generation nonvolatile memory. Trends Chem. *2*, 869–872.

44 Soni, S., Ye, G., Zheng, J., Zhang, Y., Asyuda, A., Zharnikov, M., Hong, W. and Chiechi, R. C. (2020) Understanding the role of parallel pathways via in-situ switching of quantum interference in molecular tunneling junctions. Angew. Chem. Int. Ed. *59*, 14308–14312.

45 Xu, B. and Tao, N. J. (2003) Measurement of single-molecule resistance by repeated formation of molecular junctions. Science *301*, 1221–1223.

46 Venkataraman, L., Klare, J. E., Nuckolls, C., Hybertsen, M. S. and Steigerwald, M. L. (2006) Dependence of Single-Molecule Junction Conductance on Molecular Conformation. Nature *442*, 904–907.

47 Hong, W., Li, H., Liu, S.-X., Fu, Y., Li, J., Kaliginedi, V., Decurtins, S. and Wandlowski, T. (2012) Trimethylsilyl-terminated oligo(phenylene ethynylene)s: An approach to single-molecule junctions with covalent Au–C σ-bonds. J. Am. Chem. Soc. *134*, 19425–19431.

48 Soler, J. M., Artacho, E., Gale, J. D., García, A., Junquera, J., Ordejón, P. and Sánchez-Portal, D. (2002) The SIESTA method for *ab initio* order-*N* materials simulation. J. Phys. Condens. Matter *14*, 2745–2779.

49 Ferrer, J., Lambert, C. J., García-Suárez, V. M., Manrique, D. Z., Visontai, D., Oroszlany, L., Rodríguez-Ferradás, R., Grace, I., Bailey, S. W. D., Gillemot, K. et al. (2014) GOLLUM: A next-generation simulation tool for electron, thermal and spin transport. New J. Phys. *16*, 093029.

50 Coffey, T., Bayindir, Z., DeCarolis, J. F., Bennett, M., Esper, G. and Agosta, C. C. (2000) Measuring Radio Frequency Properties of Materials in Pulsed Magnetic Fields with a Tunnel Diode Oscillator. Rev. Sci. Instrum. *71*, 4600–4606.